Science of the Total Environment 901 (2023) 165777

Contents lists available at ScienceDirect

Science of the Total Environment

journal homepage: www.elsevier.com/locate/scitotenv

Assessing urban wetlands dynamics in Wuhan and Nanchang, China

Ying Deng [a], Zhenfeng Shao [a,*], Chaoya Dang [a], Xiao Huang [b], Wenfu Wu [c], Qingwei Zhuang [a], Qing Ding [a]

[a] State Key Laboratory of Information Engineering in Surveying, Mapping and Remote Sensing, Wuhan University, Wuhan 430079, China
[b] Department of Geosciences, University of Arkansas, Fayetteville, AR 72701, USA
[c] School of Remote Sensing and Information Engineering, Wuhan University, Wuhan 430079, China

ARTICLE INFO

Editor: José Virgílio Cruz

Keywords:
Urban wetland
Fine wetland extraction
Shape features
Hierarchical decision trees
The Wetland city

ABSTRACT

Urban wetlands play a crucial role in sustainable social development. However, current research mainly focuses on specific wetland types, and fine extraction of urban wetlands remains a challenge. This study proposes a fine extraction framework based on hierarchical decision trees and shape features for urban wetlands, using Sentinel-2 remote sensing data to obtain detailed wetland data of Wuhan and Nanchang from 2016 to 2022. Our framework applies random forests to classify land cover, extracts urban fine wetlands by hierarchical decision trees and shape features, and assesses the dynamics of wetlands in the two cities. We also analyzed and discussed the characteristics of urban wetlands in the two cities. The results show that wetland accuracies of Wuhan and Nanchang are greater than 84.5 % and 82.9 %, respectively. The wetland areas of Wuhan in 2016, 2019, and 2022 are 1969.4 km^2, 1713.8 km^2, and 1681.1 km^2, while those in Nanchang are 1405.9 km^2, 1361.6 km^2, and 766.9 km^2. Inland wetlands are the main wetland types in both regions, with lake wetlands accounting for the highest proportion (over 40 %). The urban wetlands in the two cities exhibit different spatial and temporal evolution patterns, with varying change trends of wetland area and the structural proportions of fine wetlands. Besides, Wuhan's urban wetlands are primarily located in the south, while Nanchang's urban wetlands are concentrated in the east, exhibiting higher spatial and temporal dynamics. Analysis suggests that the reduced urban wetlands from 2016 to 2022 are related to fluctuating decreasing precipitation, growing population, and gross domestic product (GDP). Our study provides support for the conservation of urban wetland resources in Wuhan and Nanchang and highlights the need for targeted management strategies.

1. Introduction

Wetlands are one of the most important ecosystems on Earth, providing a range of economic and ecological functions, such as water purification, water conservation, and provision of biological habitat (Liu et al., 2013; Mitsch et al., 2015; Asselen et al., 2013; Keddy et al., 2009; Zhang et al., 2021a). Wetlands play a critical role in maintaining biodiversity, ecological security, and human well-being (Wang et al., 2012; Zhang et al., 2023a; Sahraei et al., 2023). Unlike natural wetlands, urban wetlands have unique roles due to their location in a complex urban environment (Wu et al., 2007; Savard et al., 2000; Harrison et al., 2011). In addition to regulating climate and mitigating heat island effects (Sun et al., 2012; Xue et al., 2019), urban wetlands provide tourism, vacation, and recreational areas that promote harmonious urban development (Das and Basu, 2020; Zeng et al., 2011). At the beginning of 2017, the Ramsar Convention launched the Wetland City Accreditation scheme, which is the highest achievement in the ecological protection of urban wetlands worldwide. Currently, forty-three cities around the world have been certified as Wetland Cities. However, the process of urbanization has led to the destruction of wetlands, causing serious ecological problems (He et al., 2014; Jantz et al., 2005; Zhang et al., 2007). Therefore, recognizing and protecting urban wetland resources is of paramount importance for social development.

The classification system and level are essential considerations in land cover classification. Existing land cover datasets are typically at national or global scales and the number of subcategories of wetlands is limited. Several datasets with 30 m or 10 m resolution, e.g., CLCD (Yang and Huang, 2021), GlobeLand30 (Chen et al., 2015), DW10 (Brown et al., 2022), and ESA_WC10 (Daniele et al., 2021), have only two or three categories related to wetlands, including permanent water bodies, herbaceous wetlands, and flooded vegetation. Other datasets on water or wetlands are generally classified into broad wetland categories, such

* Corresponding author.
E-mail address: shaozhenfeng@whu.edu.cn (Z. Shao).

https://doi.org/10.1016/j.scitotenv.2023.165777
Received 4 May 2023; Received in revised form 6 July 2023; Accepted 23 July 2023
Available online 29 July 2023

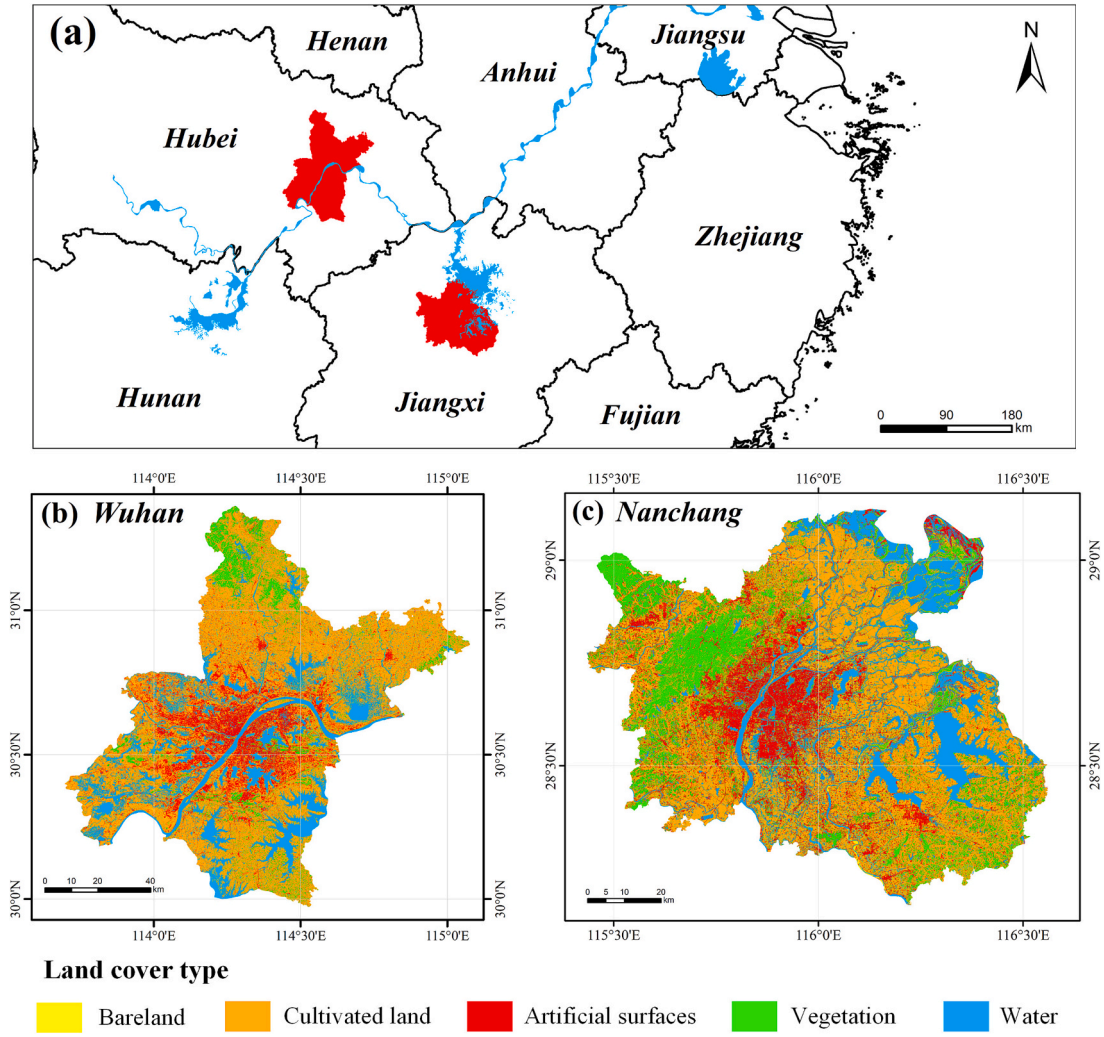

Fig. 1. Geographical location and land cover types of the study area: (a) in the vicinity of Hubei, Hunan, Jiangxi, Fujian, Zhejiang, Anhui, and Henan provinces; (b) land cover types of Wuhan; (c) land cover types of Nanchang.

as JRC_GSW (Pekel et al., 2016), HydroLakes (Messager et al., 2016), TWEA (Zhang et al., 2022), and GIC2015 (Murray et al., 2019). Due to the fragmentation and complexity of urban landscapes, detailed wetland classification data are scarce at the urban scale, limiting the rational use of urban wetlands.

In recent years, due to the abundance of remote sensing data, many studies have focused on wetland classification (Mao et al., 2020; Zhang et al., 2023b; Zhao et al., 2023; Xing et al., 2023). Remote sensing images at different temporal and spatial resolutions, including Landsat (Sheng et al., 2016), Sentinel (Jia et al., 2021; Xu et al., 2022), and MODIS (Feng et al., 2012), are widely used in wetland mapping. In addition, in order to improve the accuracy of wetland extraction, some research used multi-source remote sensing data to identify different wetlands (Zhao and Qin, 2020; Rapinel et al., 2019; Pan et al., 2022). Considering the complexity of wetlands, an appropriate method should be chosen to define the various wetlands (Adam et al., 2010). Currently, many algorithms, including random forests, object-based image analysis (OBIA), and support vector machines (SVM), had achieved wetland classification and monitoring (Wang et al., 2020a; Wang et al., 2023; Jia et al., 2021; Amani et al., 2019; Mahdavi et al., 2017). However, the complex urban environment makes it difficult to meet the needs of fine wetland classification using traditional algorithms. For example, supervised classification methods that rely solely on features, including spectral and textural features, cannot distinguish between rivers and channels (Wang et al., 2022b). There are few extraction frameworks for urban fine wetlands and it is important to incorporate other effective features, such as shape features, in the framework.

Wuhan and Nanchang, two cities located in China, have been certified as Wetland Cities in June 2022 due to their rich wetland resources and outstanding conservation efforts. In addition, Wuhan successfully hosted the 14th Meeting of the Conference of the Contracting Parties to the Ramsar Convention on Wetlands (COP14) in November 2022. However, current research on wetlands in the two cities is limited to specific wetland types or is weakly presented (Wang et al., 2008; Xu et al., 2010). For example, previous studies by Wang et al. (2008), Xu et al. (2010), Feng et al. (2012), and Li et al. (2022) focused on wetland landscape information extraction, spatial and temporal evolution, landscape patterns, and wetland pattern changes in different time frames, but they lacked fine classification and dynamic analysis of the latest urban wetland resources in Wuhan and Nanchang. As large cities in central China with similar climatic conditions, a fine wetland classification of Wuhan and Nanchang is essential for supporting the conservation and rational use of urban wetlands.

To address the research gaps identified above, this study proposes a fine extraction framework for urban wetlands using hierarchical decision trees and shape features. It should be noted that our framework focuses on wetlands within cities with water bodies as the main cover and the urban wetlands throughout the paper follow this definition. The study objectives are threefold: (1) to classify land cover accurately by applying random forests and multiple feature datasets; (2) to achieve

Table 1
Urban wetland classification system for remote sensing.

Category I	Category II	Description	MSI image example	Google Earth image example	Natural photo example
Inland wetland	Lake	Natural polygon waterbody with standing water in inland areas			
	River	Natural linear waterbody with flowing water in inland areas			
Human-made wetland	Reservoir/ pond	Artificial polygon waterbody with standing water generally with obvious dam			
	Aquaculture pond	Polygon waterbody used for aquaculture with regular shape			
	Canal/ channel	Artificial linear waterbody with flowing water generally with the obvious dam or straight boundary; Artificial rivers built for water transfer or transportation, including ditches and canals whose main aim is agricultural irrigation			
Nonwetland	Vegetation	Natural vegetation coverage area including forests, shrubs, herbaceous vegetation, artificial grassland, swamp, and marsh			
	Artificial surfaces	The surface formed by artificial construction activities, including towns and other types of residential land, industrial and mining, transportation facilities, etc.			
	Bareland	Natural cover land with less than 10 % vegetation cover, including desert, sandy land, gravel land, bare rock, saline land, etc.			
	Cultivated land	Land used for growing crops, including paddy fields, irrigated dry land, rain-fed dry land, vegetable land, and greenhouse land			

detailed classification of urban wetlands in Wuhan and Nanchang from 2016 to 2022 using the proposed framework; and (3) to evaluate and analyze the dynamics of urban wetlands in Wuhan and Nanchang during 2016–2022. The findings of this study will contribute to a better understanding of urban wetland resources, which will in turn facilitate their protection and promote sustainable development of wetland cities.

2. Data and methods

2.1. Study area

Wuhan and Nanchang are located in regions supported by the Yangtze River system throughout the year. Due to the topography, the climate, and the location, the two cities possess a dense network of water and wetland resources. In recognition of their remarkable achievements in urban wetland ecological protection, both Wuhan and Nanchang were certified as Wetland Cities in June 2022. Wuhan, the capital of Hubei province, is located between 29°58′N to 31°22′N and 113°41′E to 115°05′E, at the confluence of the Yangtze River and the Han River (Fig. 1). The region spans an area of approximately 8574 km^2, featuring flat terrain in the middle and low hills in the north and south. The subtropical monsoon climate of the region gives rise to an average annual temperature of 13–22 °C and an average annual precipitation of 1150–1450 mm. Nanchang, the capital city of Jiangxi province, is located between 28°10′N to 29°11′N and 115°27′E to 116°35′E, in the middle reaches of the Yangtze River and southwest of Poyang Lake (Fig. 1). The region is characterized by plains accounting for about 35.8 % of the total area, with rolling hills in the northwest. Nanchang experiences a subtropical monsoon climate with an average annual temperature of 16–23 °C and an average annual precipitation of 1600–1700

Table 2
Auxiliary datasets used in this study.

Product	Type	Spatial resolution	Time	Coverage	Reference
JRC Global Surface Water (JRC_GSW)	Water	30 m	1980–2020	Globe	Pekel et al. (2016)
Reservoir and Lake Surface Area Timeseries	Reservoir, Lake	–	1984–2015	Globe	Khandelwal et al. (2022)
HydroLakes	Reservoir, Lake	–	–	Globe	Messager et al. (2016)
Global River Widths from Landsat (GRWL)	River	30 m	–	Globe	Allen and Pavelsky (2018)
China's surface water bodies, Large Dams, Reservoirs, and Lakes (China-LDRL)	Reservoir, Lake	30 m	–	China	Wang et al. (2022a)
Global 30-m wetland map with a fine classification system (GWL_FCS30)	Mangrove, Swamp, Salt marsh, Tidal flat, Marsh Flooded flat, Saline	30 m	2020	Globe	Zhang et al., 2023b
ESA WorldCover (ESA_WC10)	Land cover	10 m	2020, 2021	Globe	Daniele et al. (2021)
Dynamic World (DW10)	Land cover	10 m	2015–2022	Globe	Brown et al. (2022)
Esri Land Cover (Esri_LC10)	Land cover	10 m	2017–2022	Globe	Karra et al. (2021)
GlobeLand30	Land cover	30 m	2000–2020	Globe	Chen et al. (2015)
Global land-cover product with fine classification system at 30 m (GLC_FCS30)	Land cover	30 m	2015, 2020	Globe	Zhang et al., 2021b
China land cover dataset (CLCD)	Land cover	30 m	1990–2021	China	Yang and Huang (2021)
Global artificial impervious area (GAIA)	Artificial impervious	30 m	1985–2018	Globe	Gong et al. (2020)

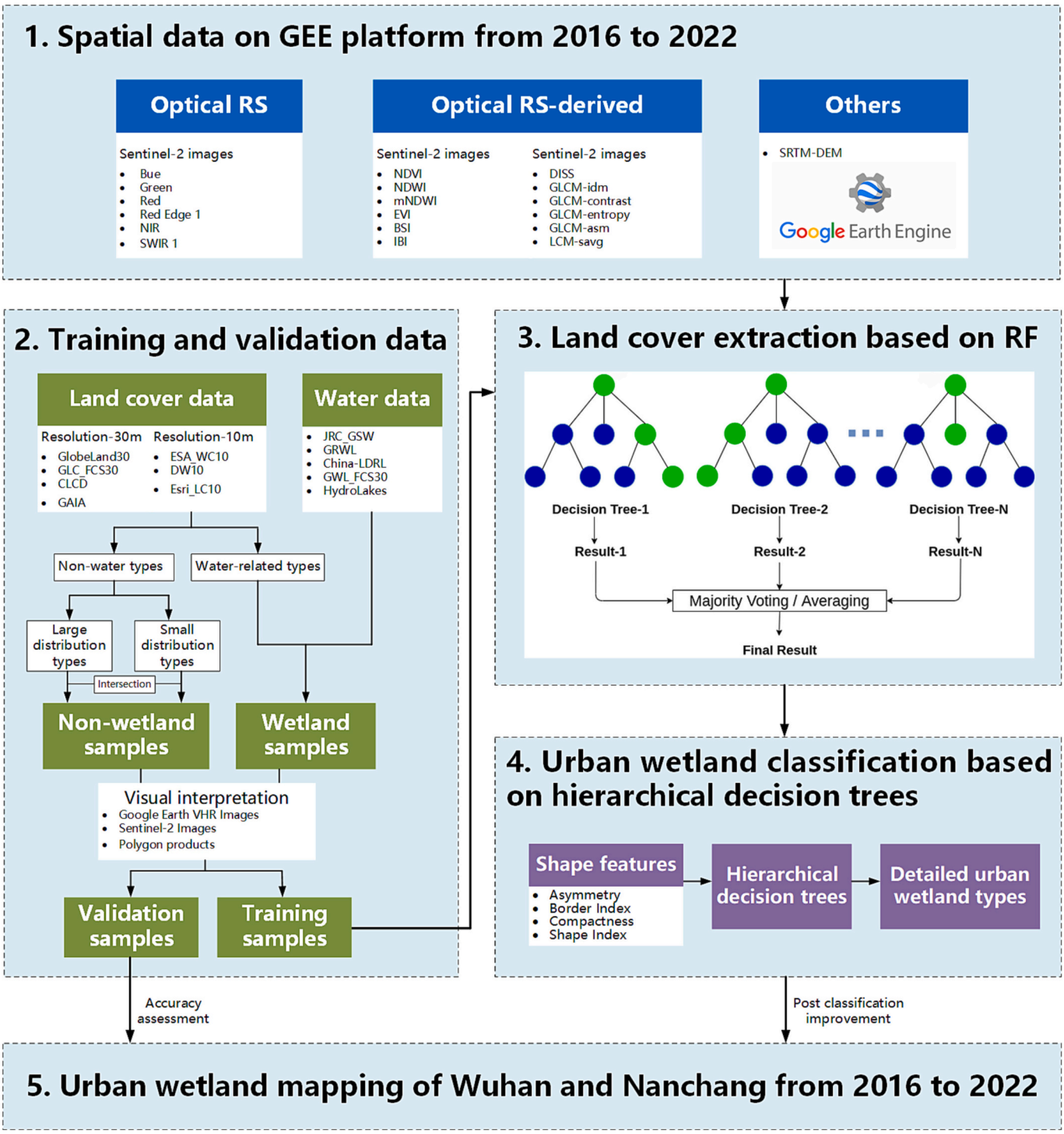

Fig. 2. The workflow of this study.

mm. In terms of social and economic factors, Wuhan has a population of 13.74 million and a total GDP of 1886.6 billion yuan in 2022, while Nanchang has a population of 6.54 million and a total GDP of 720.4 billion yuan.

2.2. *Urban wetland classification system for remote sensing*

The Ramsar Convention's definition of wetlands encompasses areas of natural or artificial, permanent or temporary marshes, peatlands, and water areas with standing or flowing fresh, brackish, and saltwater bodies, including areas of marine water with a depth at low tide not exceeding 6 m (Gong et al., 2010). As the middle reaches of the Yangtze River are abundant in water resources, this study focuses on the water component of urban wetlands. Following the Chinese wetland classification national standard (GB/T 24708-2009) and related research (Niu et al., 2009; Mao et al., 2020; Wang et al., 2022b), and considering the study's purpose and the region's characteristics, this paper classifies urban wetlands into two main categories and five subcategories, while nonwetlands are divided into four categories (Table 1). Coastal wetlands are not included in the study area, and inland swamps and marshes are excluded from the classification system due to their high vegetation cover. Additionally, paddy fields have been classified as nonwetlands.

Table 3
List of features used for land cover classification.

Feature type	Parameters	Definition or description
Band features	B2	Blue band
	B3	Green band
	B4	Red band
	B5	Red Edge 1 band
	B8	NIR band
	B11	SWIR 1 band
Index features	NDVI	(B8 − B4) / (B8 + B4)
	NDWI	(B3 − B8) / (B3 + B8)
	mNDWI	(B3 − B11) / (B3 + B11)
	EVI	2.5 * ((B8 − B4) / (B8 + 6 * B4 − 7.5 * B2 + 1))
	BSI	((B4 + B11) − (B8 + B2)) / ((B4 + B11) + (B8 + B2))
	IBI	(2 * B11 / (B11 + B8) − (B8 / (B8 + B4) + B3 / (B3 + B11))) / (2 * B11 / (B11 + B8) + (B8 / (B8 + B4) + B3 / (B3 + B11)))
Texture features	DISS	Dissimilarity
	GLCM-idm	Inverse Difference Moment; Measures the homogeneity
	GLCM-contrast	Measures the local variations
	GLCM-entropy	A statistical measure of randomness
	GLCM-asm	Angular Second Moment; Measures the number of repeated pairs
	GLCM-savg	Sum Average
Topographic features	Elevation	SRTM-DEM data with a resolution of 30 m

2.3. Data sources and preprocessing

Sentinel-2 is an Earth observation mission implemented as part of the Copernicus program by the European Space Agency to provide remote sensing observations of the Earth's surface. The mission comprises two satellites, Sentinel-2A and Sentinel-2B, equipped with a multi-spectral instrument capable of capturing images in 13 bands, with a spatial resolution of 10 m and a revisit period of 5 days. Given the seasonal variation in climate affecting Wuhan and Nanchang, with flood seasons in summer and autumn, during which urban wetland resources are replenished, this study was restricted to the period from June to October. Moreover, given the potential for cloudy and rainy weather to affect image quality, we filtered images with cloud cover of less than 0.75 % and masked out clouds using the QA60 bitmask band on the Google Earth Engine (GEE) platform. Ancillary data used in this study, including different wetland categories datasets, land cover data, and other relevant data sources, are presented in Table 2 and were primarily used to generate the sample points.

2.4. Methods

The extraction process of the urban fine wetland in this study, as shown in Fig. 2, consists of five major steps: 1) collection and preprocessing of spatial data from 2016 to 2022 based on the GEE cloud platform; 2) acquisition of training and validation samples; 3) land cover extraction based on random forests; 4) urban wetland classification based on hierarchical decision trees and shape features; 5) urban wetland mapping in Wuhan and Nanchang during 2016–2022.

2.4.1. Acquisition of training and validation samples

In the context of remote sensing interpretation, the manual selection of sample points can be prone to subjective influence due to the reliance on individual experience and knowledge, resulting in a high workload. To minimize the effect of human subjectivity and ensure a balance between accuracy and workload for sample collection, this study employed published datasets and combined them with visual interpretation and Google Earth Very High-Resolution (VHR) images to establish training and validation samples. Specifically, the study selected 8119 and 7572 samples in Wuhan and Nanchang, respectively, and used 70 % of the samples for training and 30 % for validation purposes.

Table 4
Shape features used for urban wetland classification.

Shape features	Expression	Definition or description
Asymmetry	L / W	Describes the relative length of the element compared to a normal polygon. The larger the value is, the higher the asymmetry is.
Border Index	BL / 2 *(L + W)	Represents the smoothness of an element and also the degree of approximation of the element to the minimum bounding rectangle in terms of circumference.
Compactness	AP / (L *W)	Describes the degree of similarity of the element to the minimum bounding rectangle in terms of area.
Shape Index	BL / (4 *$\sqrt{AP}$)	Describes the smoothness of the element boundary. The more broken the element is, the larger the shape index is.

Note: BL-the border length of the element; AP-the area pixel of the element; L-the length of the minimum bounding rectangle; W-the width of the minimum bounding rectangle.

We categorized land cover datasets into water and non-water categories and randomly sampled categories with large and concentrated distributions in non-water areas, such as cultivated land and artificial surfaces, from the intersection of land cover datasets at a 30 m resolution. Additionally, small distributed categories were sampled using ESA_WC10, DW10, and Esri_LC10. The sample categories were further examined using Google Earth VHR images and visual interpretation. Samples of water areas were obtained from water-related datasets and water categories collected from land cover products. It is important to note that in the event of missing datasets, adjacent years were used, and the data were verified using Google Earth.

2.4.2. Extracting land cover based on random forests

In the field of machine learning, the random forests classifier, consisting of multiple decision trees, is widely applied in remote sensing classification (Mutanga et al., 2012; Amani et al., 2019; Yue et al., 2023; Feng et al., 2022). In this study, we utilized the random forests algorithm to classify land cover on the GEE platform. The feature importance ranking and the optimal number of decision trees used in the classification process are presented in Figs. S1 and S2, respectively.

Based on existing studies (Mao et al., 2020; Xing et al., 2023; Wang et al., 2022b), we chose four types of features for the classification process, including band features, index features, texture features, and topographic features (Table 3). Band features included six bands, namely B2, B3, B4, B5, B8, and B11. Index features were based on various bands and included the normalized difference vegetation index (NDVI) (Rouse et al., 1973), enhanced vegetation index (EVI) (Huete et al., 1997), normalized difference water index (NDWI) (Mcfeeters, 1996), modified normalized difference water index (mNDWI) (Xu, 2006), bare surface index (BSI) (Rikimaru, 1996), and index-based built-up index (IBI) (Xu, 2008). Texture features calculated five Grey-Level Co-occurrence Matrix (GLCM) (Haralick et al., 1973) metrics and an additional metric (Conners et al., 1984). In addition, we also considered topographic features, i.e., elevation, in this study.

2.4.3. Detailed urban wetland classification based on hierarchical decision trees and shape features

In remote sensing tasks, hierarchical decision trees can be utilized to achieve classification through a series of if-then rules based on expert experience and prior knowledge (Mao et al., 2020; Wang et al., 2020a; Wang et al., 2020b). The shape characteristics of wetlands vary widely, where linear water bodies such as rivers and canals are characterized by their elongated shapes, while lakes, reservoirs, and aquaculture ponds are identified as polygon-shaped bodies or regular patches. This study achieved a fine classification of wetlands using hierarchical decision

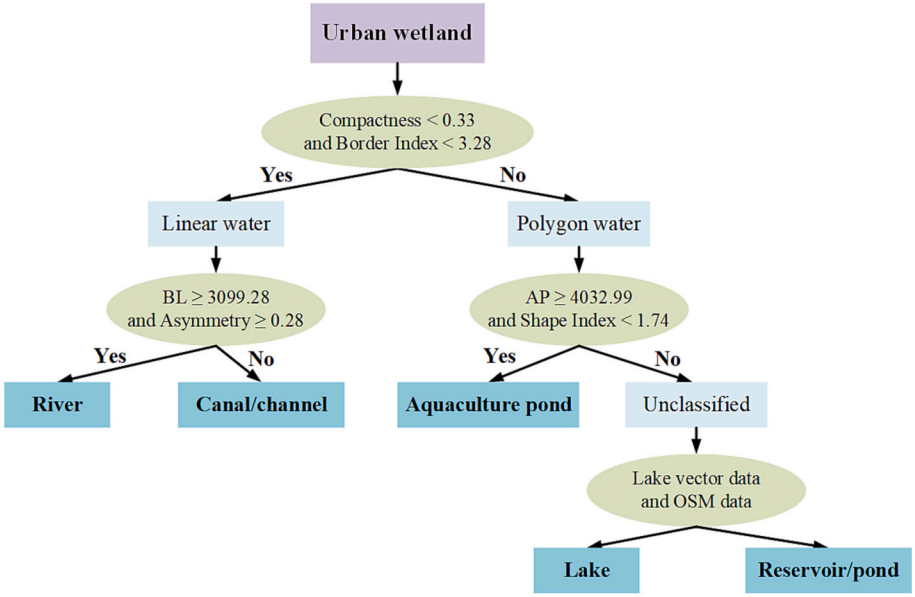

Fig. 3. An example of the hierarchical decision tree for urban wetland classification.

Table 5
Classification accuracy (%) of different land cover categories for Wuhan and Nanchang.

		Wuhan						Nanchang					
		2016		2019		2022		2016		2019		2022	
Category I	Category II	UA	PA	UA	PA	UA	PA	UA	PA	UA	PA	UA	PA
Inland wetland	River	84.2	84.2	84	95.5	81.3	86.7	91.3	95.5	93.9	91.2	85.7	90
	Lake	85.7	82.8	86.7	90.7	95.1	86.7	91.3	91.3	85.7	90	89.3	86.2
Human-made wetland	Reservoir/ pond												
	Canal/ channel	85.7	85.7	93.3	77.8	83.3	76.9	94.1	88.9	80	85.7	86.7	81.3
	Aquaculture pond	82.8	85.7	90	85.7	78.6	91.7	87.5	87.5	84.6	78.6	75.0	80
Nonwetland	Vegetation	97.8	89.8	97.2	90.8	100	97.1	96.3	96.3	95.5	90	84.6	91.7
	Artificial surfaces	95.3	96.2	85.5	84.7	84.7	87.2	97.7	97.7	92.4	97.6	96.1	96.8
	Bareland	100	91.7	91.7	93.6	86.4	80.9	96.4	96.4	100	89.3	97.2	97.2
	Cultivated land	89	94.7	88.1	91.4	92.6	95.7	97.3	96.1	94.9	97.9	94.4	90.6
	WA	84.5		88		86.6		91.1		87.8		82.9	
	OA	95.1		92		92.4		96.8		92.3		95	
	Kappa	93.6		88.9		89.4		95.9		93.8		93.4	

trees and shape features. The shape features used in this study are presented in Table 4, which includes asymmetry, border index, compactness, and shape index. Based on the characteristics of different wetland types, we classified urban wetlands using ArcGIS 10.7 and Matlab 2019a. Given the influence of different times and cities on water body distribution, it is inappropriate to distinguish wetland categories using a static threshold. In this study, we presented the specific classification rules of the decision tree for Wuhan in 2022, as illustrated in Fig. 3.

2.4.4. Accuracy assessment and post classification improvement

In this study, the overall accuracy (OA), producer's accuracies (PA), user's accuracies (UA), and kappa coefficient were utilized to evaluate the classification accuracy based on the confusion matrix. Furthermore, wetland accuracy (WA) was used to measure the accuracy of wetland categories, defined as the ratio of the number of correctly classified wetlands to the total number of wetland samples.

Given the complexity of urban surfaces and wetland types, accurate classification using spectral and shape characteristics can be challenging in urban areas (Mao et al., 2020; Wang et al., 2022b). To improve classification accuracy and reflect the realistic distribution, this study combined visual interpretation and Google Earth VHR images to correct misclassified categories and inaccurate boundaries. For instance, urban building shadows and mountain shady slopes that were mistakenly classified as water bodies were revised accordingly. In wetland classification, adjacent polygons with a distance of less than one pixel were misclassified as a whole, affecting the shape characteristics of the polygon element. To address this issue, we performed clipping in ArcGIS 10.7 based on the actual situation to improve classification accuracy.

3. Results

3.1. Classification accuracy

The classification accuracy for land cover in Wuhan and Nanchang, as evaluated by OA and the kappa coefficient, is greater than 92 % and 88.9 %, respectively. Additionally, the WA for Wuhan and Nanchang is above 84.5 % and 82.9 %, respectively, as presented in Table 5. The UA and PA for inland wetlands in both areas exceed 81.3 % and 82.8 %, respectively, with accuracies mainly above 85.7 %. Notably, the PA of rivers reached 95.5 % for 2019 in Wuhan and 2016 in Nanchang, while the UA of lakes for Wuhan in 2022 is 95.1 %. The classification accuracy of human-made wetlands in both areas is low, with poor accuracies for aquaculture ponds, mainly because of misclassification as ponds. Additionally, canal/channels in urban areas are fewer and narrower, and elements with less than one pixel are prone to misclassification. The UA and PA for nonwetland categories exceeded 84.6 % and 80.9 %,

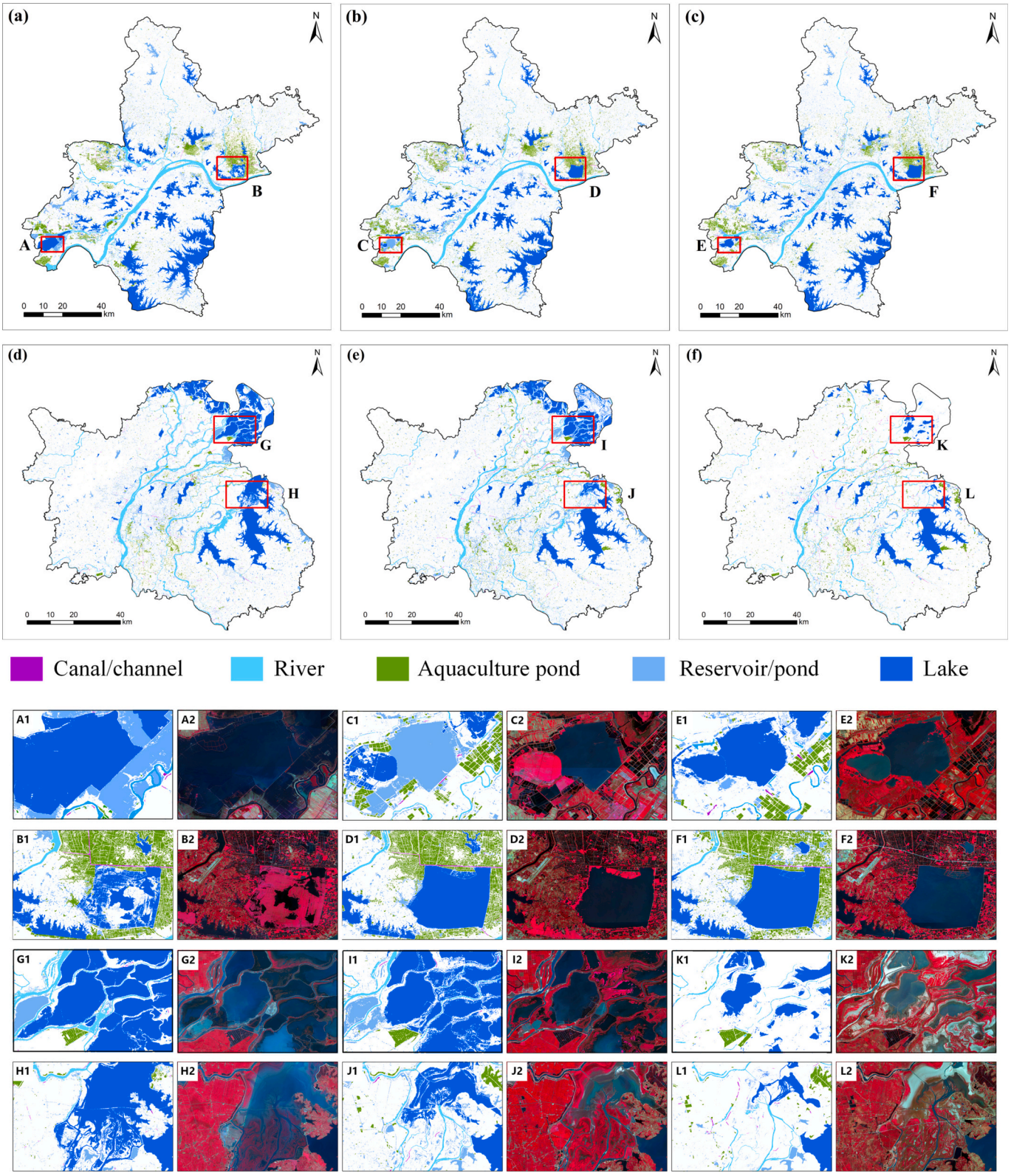

Fig. 4. Urban wetland mapping for Wuhan (a, b, c) and Nanchang (d, e, f) in 2016, 2019, and 2022. (A1–F2) Results of fine wetland classification and MSI images in the Chen Lake region of Wuhan in 2016, 2019, and 2022, (G1–L2) Results of fine wetland classification and MSI images in the Poyang Lake region of Nanchang in 2016, 2019, and 2022.

respectively. In summary, the accuracy of wetland classification was considered satisfactory for both sites.

3.2. Dynamics of urban wetlands in Wuhan and Nanchang

This study employed hierarchical decision trees and shape features to extract urban wetlands in Wuhan and Nanchang from 2016 to 2022, as

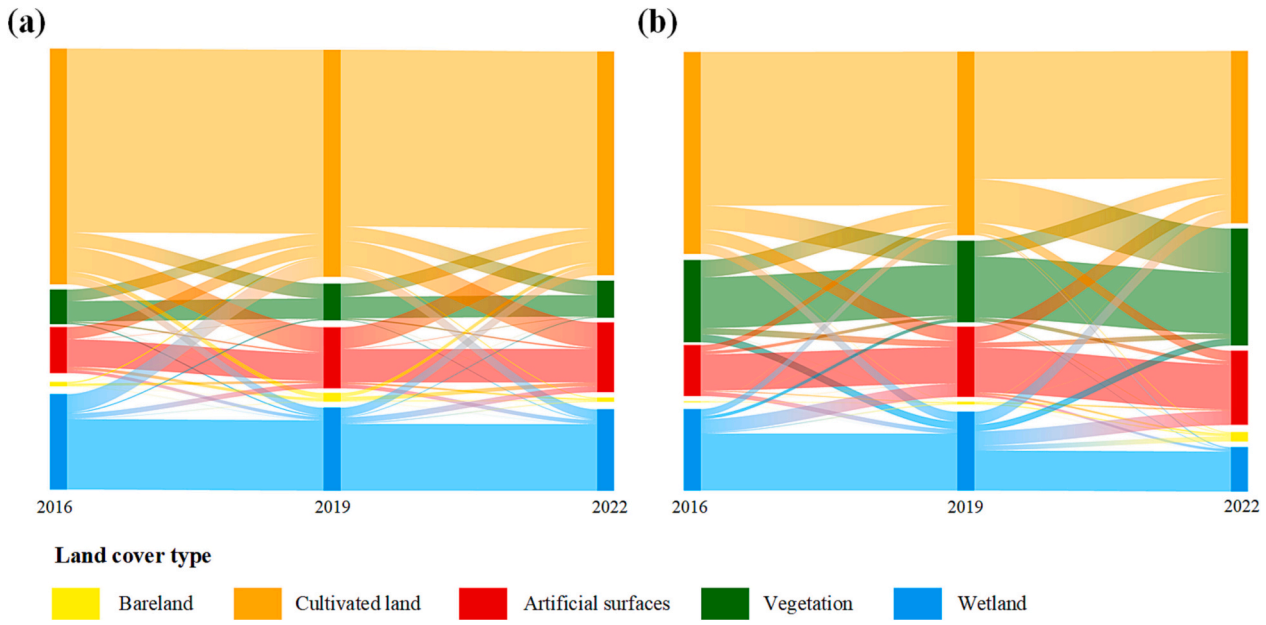

Fig. 5. Sankey diagram of land cover dynamics in Wuhan (a) and Nanchang (b) from 2016 to 2022.

depicted in Fig. 4. Wuhan has extensive wetlands with numerous lakes and rivers, and aquaculture ponds are mainly located around the lakes. The interannual variation is more pronounced in areas with mixed distribution of multiple wetland types, such as Chen Lake in the southwest corner (Fig. 4A1, C1, E1). In Nanchang, the wetlands are mainly concentrated in the north and east, with many rivers passing through the city. Compared with 2016 and 2019, there was a clear shrinking trend of wetlands in Nanchang in 2022, with a substantial decrease in lake wetlands in the north (Fig. 4G1, I1, K1), possibly related to the dry weather in that year, as reported by Jia et al. (2023) and Guan and Zeng (2022).

Table S1 displays the area statistics of each wetland type. The wetland areas of Wuhan in 2016, 2019, and 2022 are 1969.4 km^2, 1713.8 km^2, and 1681.1 km^2, respectively, while those in Nanchang are 1405.9 km^2, 1361.6 km^2, and 766.9 km^2, respectively. Canal/channels have the smallest area, while lake wetlands have the largest, followed by reservoir/ponds and rivers. The area of lake wetlands in Wuhan decreased from 908.37 km^2 in 2016 to 745.41 km^2 in 2022, whereas in Nanchang, it reduced from 646.16 km^2 to 311.78 km^2. Inland wetlands are the dominant wetland type in both study areas, with 986.54 km^2 and 496.39 km^2 in Wuhan and Nanchang in 2022, respectively.

3.3. Conversions between urban wetlands and other land cover types

In this study, the land cover results for the two regions from 2016 to 2022 were obtained using random forests and four features. We mapped the sankey diagram of land cover dynamics in Wuhan and Nanchang from 2016 to 2022, as depicted in Fig. 5. Besides, the transfer matrix was used to quantify land cover changes and transformations (Table S2, S3, S4, S5).

During the study period, the highest conversion ratio between cultivated land and wetlands was observed in Wuhan, followed by artificial surfaces and wetlands (Fig. 5). Specifically, 374.71 km^2 and 105.30 km^2 of wetlands were converted to cultivated land and artificial surfaces from 2016 to 2019, respectively (Table S2). By contrast, 159.63 km^2 of cultivated land was turned into wetlands. Table S3 showed that during 2019–2022, the conversion of cultivated land to wetlands increased to 203.04 km^2. The conversion of wetlands to other land cover types decreased compared to the previous three years. Overall, urban wetlands in Wuhan exhibited relative stability, showing a small decreasing trend. Different from Wuhan, in addition to artificial surfaces and cultivated land, vegetation was also a land cover type with a large area of wetland conversion. From 2016 to 2019, 159.63 km^2 of vegetation was transformed into urban wetlands. And during 2019–2022, 118.93 km^2 of wetlands were converted back to vegetation. Notably, the wetland area of Nanchang in 2022 significantly decreased compared to 2016, with a large number of wetlands converted to other land cover types.

4. Discussion

4.1. Comparing urban wetlands derived from this study with other land cover datasets

To validate the effectiveness of the wetland mapping extraction framework, Fig. 6 compares the wetlands derived from this study with other two datasets with the same 10 m spatial resolution, namely DW10 and Esri_LC10. The comparison demonstrates that the results of this study are highly accurate and better reflect the actual distribution of land cover. Firstly, the wetland classification system in this study was established based on the Chinese wetland classification national standard (GB/T 24708-2009) and relevant wetland research in China (Niu et al., 2009; Mao et al., 2020; Wang et al., 2022b), which is in line with the relevant wetland definition of the Ramsar Convention and has ecological conservation significance. Specifically, urban wetlands are classified into two categories, namely inland wetlands and human-made wetlands, and five subcategories, namely lake, river, reservoir/pond, canal/channel, and aquaculture pond. In contrast, the other datasets are designed for land cover classification and area assessment. With respect to wetland categories, DW10 and Esri_LC10 only have two categories, water, and flooded vegetation.

Moreover, as depicted in Fig. 6, the results of this study present spatial details more accurately. In the Wuhan example area (row 1), the edges of aquaculture ponds and canal/channels are clearly identified, which reflects the surface distribution more realistically. In contrast, the water bodies of DW10 show contiguous fragmentation, and Esri_LC10 is more homogeneous with rougher wetland edges. In the Nanchang example area (row 4), DW10 misclassifies most of the area as flooded vegetation. The results of this paper are in good agreement with Esri_LC10, but the latter is limited by the classification system and does

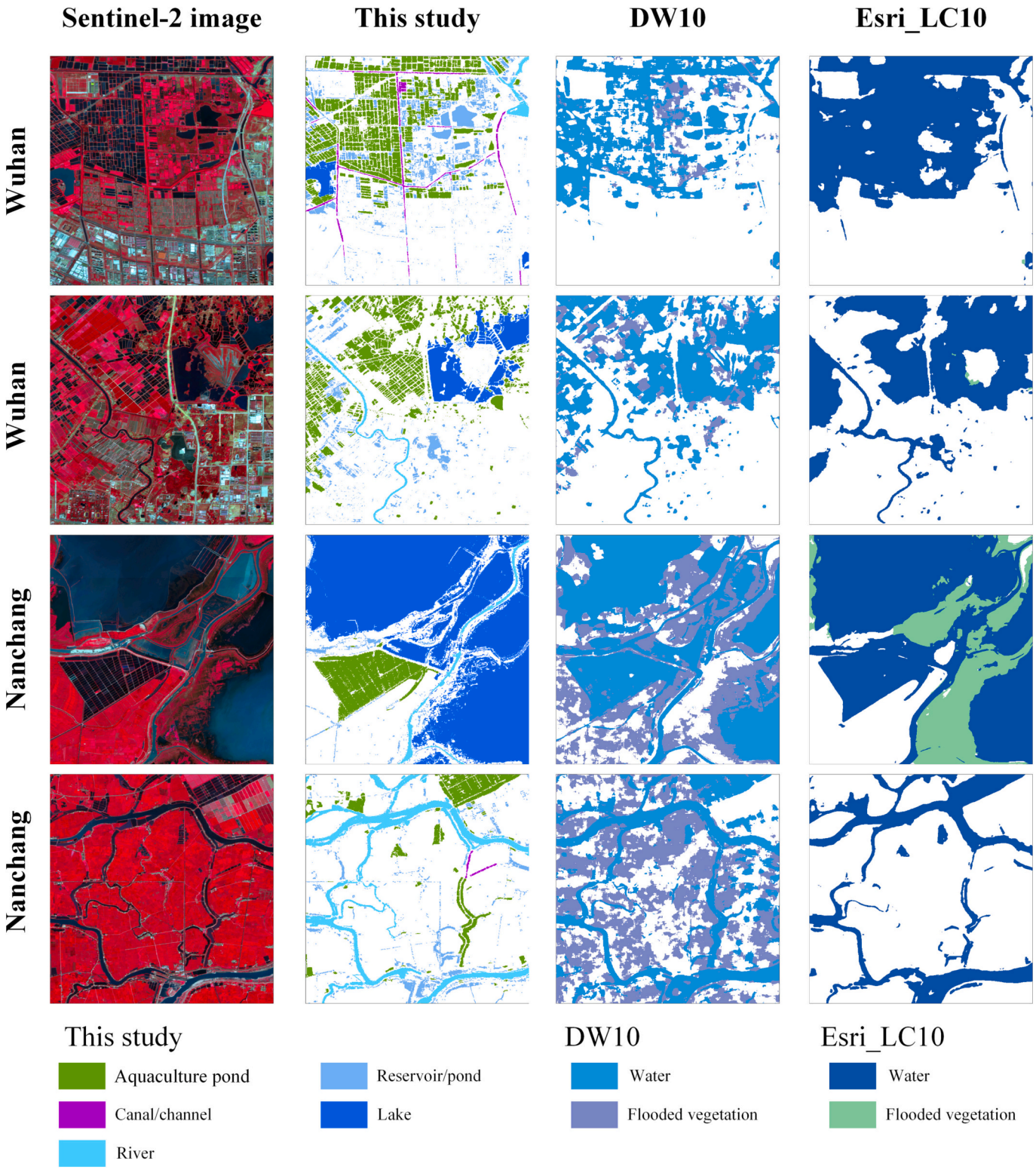

Fig. 6. Comparison of wetlands derived from this study with DW10, Esri_LC10 in selected areas in Wuhan and Nanchang.

not distinguish between lakes, rivers, and aquaculture ponds. Overall, the fine wetlands extracted using the method in this paper are more suitable for wetland conservation in terms of classification systems and have better performance in preserving spatial details.

4.2. Urban wetland analytics between Wuhan and Nanchang

The analysis of proportional changes in land cover, fine wetlands, and Category I (Table 1) features in Wuhan and Nanchang urban wetlands reveals distinct spatial and temporal evolution patterns, as illustrated in Fig. 7. Notably, the two regions exhibit the following differences: First, while both cities experienced a decline in wetland

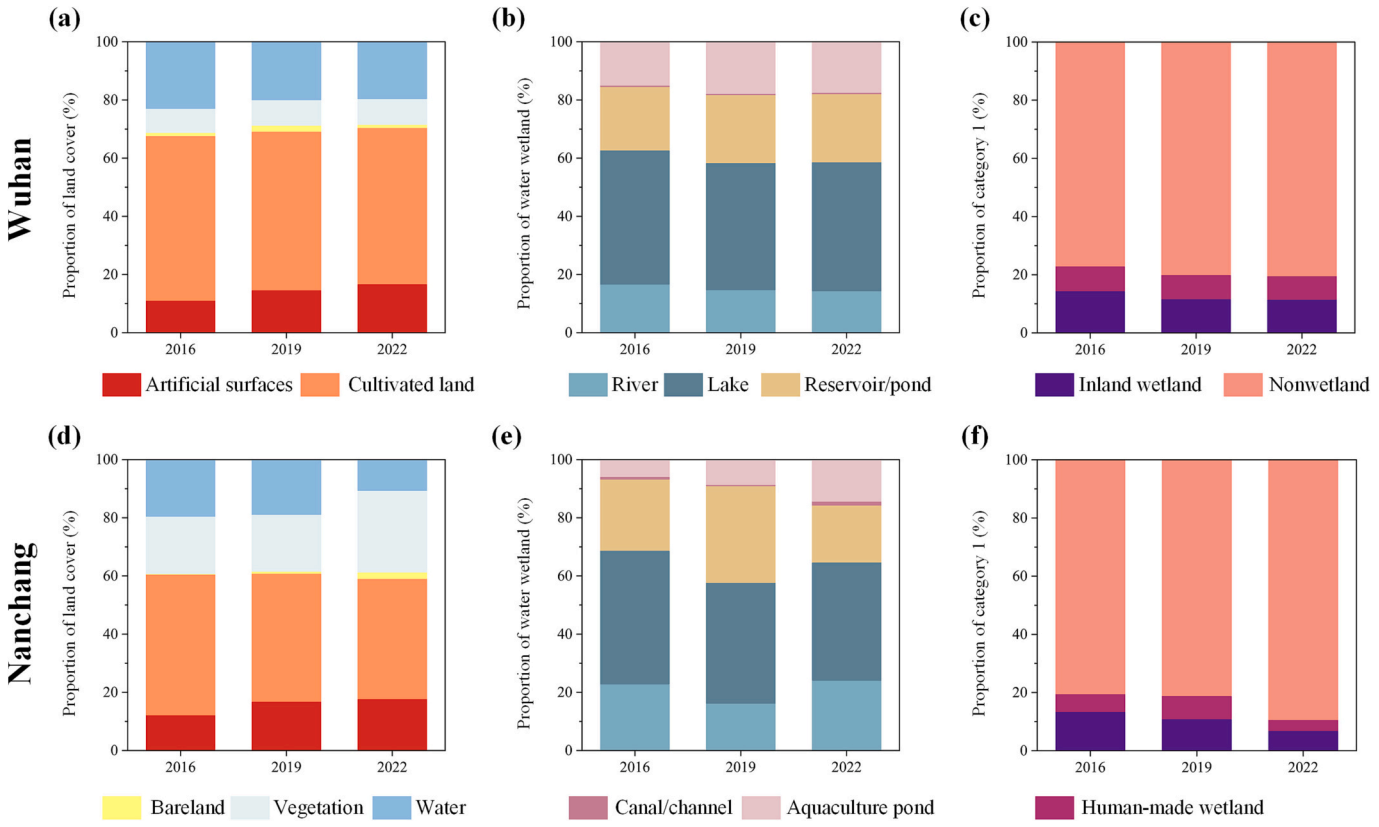

Fig. 7. The proportion of land cover, detailed urban wetland, and Category I in Wuhan and Nanchang.

areas over the study period, Wuhan's wetland area decreased at a shallower rate compared to Nanchang, which experienced a significant drop in 2022. Second, the structural proportions of fine wetlands differ between the two regions, with Wuhan having a higher proportion of aquaculture pond areas and lower percentages of canals/channels and rivers, which accounted for less than 20 % in all cases. In contrast, Nanchang had a higher percentage of rivers, accounting for over 20 % in 2016 and 2022. Both cities had lake wetlands as the dominant wetland type, comprising over 40 % of the total wetland area. Third, Fig. 7c, 7f demonstrate that in both places, the proportions of the three types of Category I from high to low are nonwetland, inland wetland, and human-made wetland, and the proportion of nonwetland is close to or exceeds 80 %. Furthermore, while there was no significant change in the human-made wetlands and inland wetlands in Wuhan from 2016 to 2022, Nanchang witnessed a significant decrease in these features in 2022.

Fig. 8 presents an analysis of the spatial characteristics of wetlands in Wuhan and Nanchang through a count of water body inundation and wind-rose diagrams. The wetlands in the two regions display different spatial distributions and water body inundation patterns. In Wuhan, hills and woodlands are situated in the north, resulting in the concentration of wetlands mainly in the south. Conversely, Nanchang's urban wetlands are primarily located in the eastern part of the city, influenced by the mountains in the northwest. Notably, the wetlands in the northeastern region near Poyang Lake, the largest freshwater lake in China, have the widest distribution in Nanchang. Fig. 8a and Fig. 8b indicate that the water level fluctuation areas, defined as the number of water inundations of a single pixel being 1 or 2, are typically located near large lakes in both regions. However, the Poyang Lake wetlands exhibit high spatial and temporal dynamics, with a large interannual variation of water body inundation area and less distribution of permanent water body area, defined as the number of water inundations of a single pixel being 3. Statistical analysis indicates that the proportion of permanent water body area in Wuhan, at 14.6 %, is significantly higher than that in Nanchang, which is 8.5 %.

To summarize, we observe that wetland evolution in regions with similar geographical and climatic conditions can differ significantly. Specifically, Wuhan and Nanchang, two central Chinese cities that share the Yangtze River system and subtropical monsoon climate, exhibit heterogeneity in wetland evolution both temporally and spatially. This finding underscores the importance of site-specific analysis in understanding wetland dynamics and the need for targeted conservation and management strategies to preserve this critical ecosystem.

4.3. The impact of natural and artificial factors on urban wetland dynamics

To explore the drivers of wetland dynamics, we considered six possible factors that include annual average precipitation, temperature, annual total sunshine duration, rainfall time, gross domestic product (GDP), and population, displayed in Fig. 9 and Table S6.

The meteorological data indicate a noticeable increase in overall precipitation (Fig. 9b) and the total duration of precipitation (Fig. 9d) in Wuhan and Nanchang, accompanied by a decline in the duration of sunshine (Fig. 9c). Notably, Nanchang has experienced a more pronounced increase in precipitation. Moreover, the average annual temperature in Nanchang has continued to rise at a consistent rate of 0.06 °C per year from 2003 to 2022 (Fig. 9a), which is consistent with the global trend of warming (Coumou and Rahmstorf, 2012; Dang et al., 2022). It is worth mentioning that the precipitation in both areas displayed a decreasing trend from 2016 to 2019, in line with the decrease in the total amount of wetlands (Table S6). From 2019 to 2022, there was a surge in precipitation, peaking in 2020, and then declining. In 2022, Nanchang experienced a sharp drop in precipitation, accompanied by a significant decrease in its wetland area, indicating a possible link between climate factors and wetlands.

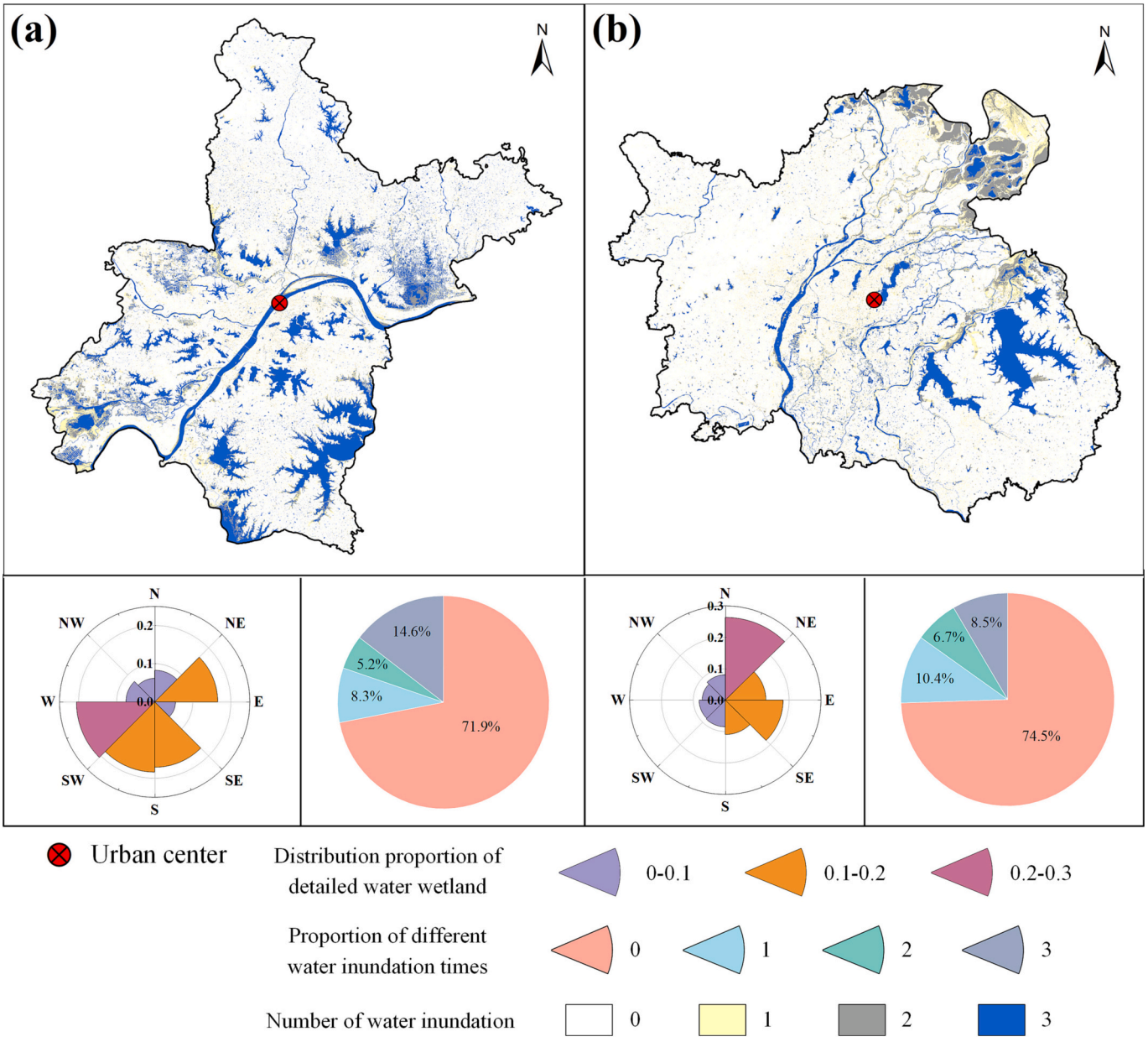

Fig. 8. The distribution of urban wetlands, water inundation times, and their proportions in Wuhan (a) and Nanchang (b).

China's accelerating urbanization process, accompanied by a surging urban population, has been a key driver of economic growth. Over the period 2001–2022, the population of Wuhan and Nanchang increased significantly by 68.8 % and 49.2 %, respectively (Fig. 9e), while their GDP experienced rapid growth (Fig. 9f). This urban expansion has led to changes in land cover, with the natural land being replaced by infrastructure (Huang et al., 2018; Hadeel et al., 2009; Shao et al., 2020; Cai et al., 2022). This development has given rise to several ecological problems that have necessitated the implementation of various environmental protection policies, including the 'Natural Forest Conservation Program' (NFCP) and the 'Returning Farmland to Lake Program' (RFLP) (Luo et al., 2019). Notably, both Wuhan and Nanchang have made significant efforts to conserve their wetland resources, with several internationally important wetlands and wetland conservation parks. However, despite these efforts, the GDP and population of both cities continued to grow between 2016 and 2022, leading to an increase in the demand for water consumption. Furthermore, natural factors such as fluctuating precipitation and rising temperatures, coupled with urban expansion, have contributed to a certain degree of decrease in urban wetland areas.

4.4. Limitations and potential improvements of this study

This study utilized hierarchical decision trees and shape features to achieve a fine classification of wetlands in Wuhan and Nanchang. However, it is essential to recognize several limitations. First, the shadows of buildings in urban areas and shady slopes in mountainous areas can be less bright, leading to potential misclassification as water bodies in the remote sensing images (Fig. 10a, b). While manual correction was carried out in this study, the correction coverage area is limited, and further methods to eliminate shadows need to be considered in future research. Second, the spatial resolution of remote sensing images restricts the accurate extraction of wetlands with small spatial scales in complex urban environments. For instance, canals or channels with a width of less than one pixel cannot be extracted (Fig. 10c, d). Additionally, when performing fine wetland classification, the shape

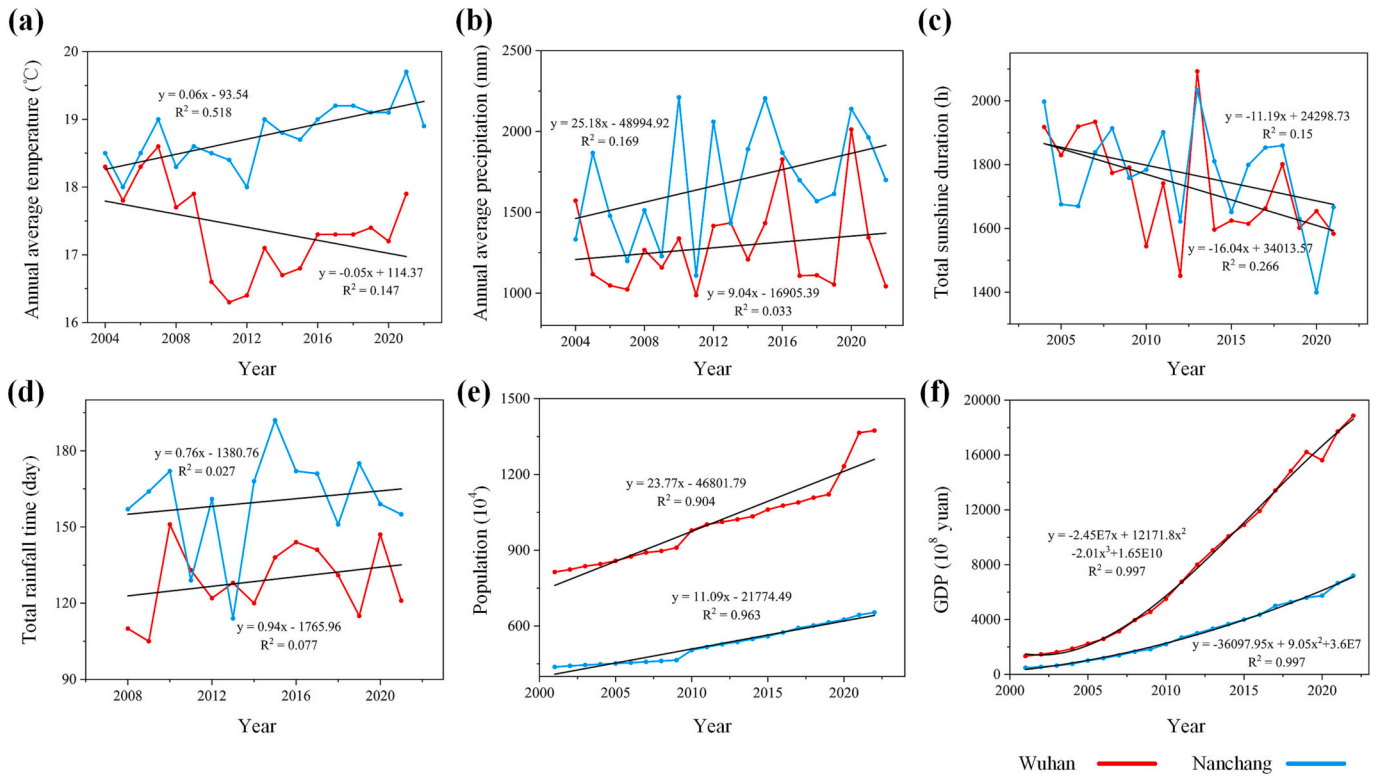

Fig. 9. Dynamics of annual average precipitation (a), temperature (b), annual total sunshine duration (c), rainfall time (d), population (e), and GDP (f) in Wuhan and Nanchang.

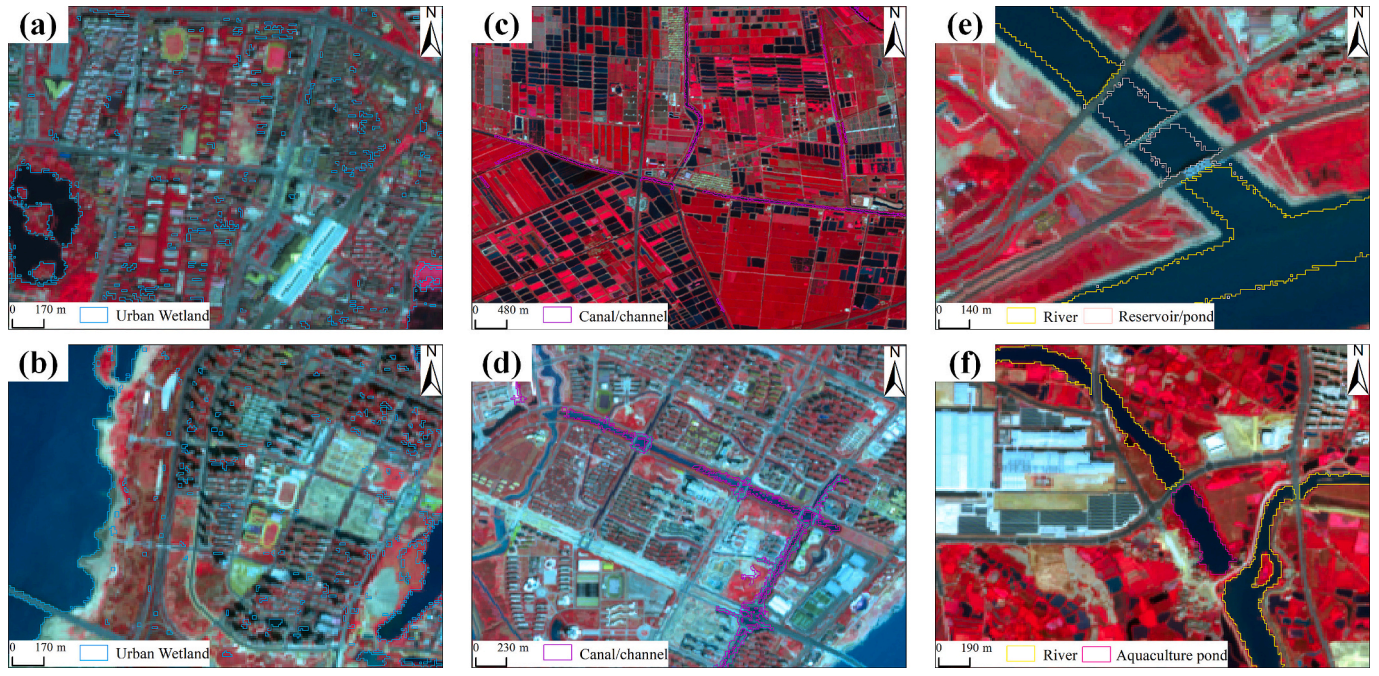

Fig. 10. The limitation examples of this study. (a) MSI image and urban wetlands in Wuhan. (b) MSI image and urban wetlands in Nanchang. (c) MSI image and canal/channels in Wuhan. (d) MSI image and canal/channels in Nanchang. (e) MSI image and classification results in Wuhan. (f) MSI image and classification results in Nanchang.

features of polygon elements can be influenced by the urban environment. Artificially constructed bridges, for instance, can interfere with the integrity of rivers and lakes, introducing some uncertainty into the classification (Fig. 10e, f).

5. Conclusions

This study proposes a framework for the fine extraction of urban wetlands based on hierarchical decision trees and shape features, utilizing Sentinel-2 as the primary data source to obtain detailed wetland

information for Wuhan and Nanchang between 2016 and 2022. The land cover classification is achieved by applying random forests and multi-feature sets, followed by the mapping of urban fine wetlands using hierarchical decision trees and shape features. The dynamics of wetlands in Wuhan and Nanchang are then characterized and comparatively analyzed. The results indicate that the wetland accuracies of Wuhan and Nanchang are greater than 84.5 % and 82.9 %, respectively. The wetland areas in Wuhan for 2016, 2019, and 2022 are 1969.4 km^2, 1713.8 km^2, and 1681.1 km^2, respectively, while those in Nanchang are 1405.9 km^2, 1361.6 km^2, and 766.9 km^2, respectively. Inland wetlands are the main wetland types in both areas, with lake wetlands accounting for the highest proportion (over 40 %). Compared with the DW10 and Esri_LC10 datasets, the results of urban wetlands in this study exhibit higher accuracy and better reflect the actual distribution of the surface.

Further analysis reveals that the urban wetlands in Wuhan and Nanchang display distinct spatial and temporal evolution patterns, reflected in three aspects: (1) differing trends in the area of urban wetlands; (2) varying structural proportions of fine wetlands; and (3) certain similarities and differences in the structure of inland wetland, human-made wetland, and nonwetland. Moreover, this study shows that the decrease in urban wetlands between 2016 and 2022 is linked to fluctuating declining precipitation, continuous population growth, and increasing GDP. In 2022, a clear trend of shrinking urban wetlands is observed in Nanchang. Overall, this study provides insights into recognizing and protecting urban wetland resources and promoting sustainable development in wetland cities.

CRediT authorship contribution statement

Ying Deng: Data curation, Methodology, Software, Formal analysis, Writing - original draft. Zhenfeng Shao: Methodology, Supervision, Funding acquisition. Chaoya Dang: Methodology, Data resources, Writing - review & editing. Xiao Huang: Writing - review & editing. Wenfu Wu: Conceptualization, Methodology. Qingwei Zhuang: Writing - review & editing. Qing Ding: Conceptualization, Methodology.

Declaration of competing interest

The authors declare that they have no known competing financial interests or personal relationships that could have appeared to influence the work reported in this paper.

Data availability

The Sentinel-2 remote sensing images are available from https://developers.google.com/earth-engine/datasets/catalog/sentinel-2. The Dynamic World V1 datasets are available from https://developers.google.com/earth-engine/datasets/catalog/GOOGLE_DYNAMICWORLD_V1. The Esri Land Cover datasets are available from https://www.arcgis.com/home/item.html?id=cfcb7609de5f478eb7666240902d4d3d. The annual average precipitation, temperature, annual total sunshine duration, rainfall time, gross domestic product (GDP) data are available from https://ceidata.cei.cn/, https://tjj.wuhan.gov.cn/tjfw/tjnj/ and http://tjj.nc.gov.cn/ncstjj/tjgb/nav_list.shtml.

Acknowledgments

This work was supported in part by the National Natural Science Foundation of China under Grants 42090012; Guangxi Science and Technology Program under Grants 2021AB30019; Hubei Key R & D Plan under Grants 2022BAA048; Sichuan Science and Technology Program under Grants 2022YFN0031, 2023YFS0381, and 2023YFN0022; Zhuhai Industry University Research Cooperation Project of China under Grants ZH22017001210098PWC; Shanxi Science and Technology Major Special Project under Grants 202201150401020; Guangxi Key Laboratory of Spatial Information and Mapping Fund Project under Grants 21-238-21-01. We thank Wuhan Geomatics Institute for providing the hydrological vector data of Wuhan. We thank the academic editors and reviewers for their kind suggestions and valuable comments.

Appendix A. Supplementary data

Supplementary data to this article can be found online at https://doi.org/10.1016/j.scitotenv.2023.165777.

References

Adam, E., Mutanga, O., Rugege, D., 2010. Multispectral and hyperspectral remote sensing for identification and mapping of wetland vegetation: a review. Wetl. Ecol. Manag. 18, 281–296. https://doi.org/10.1007/s11273-009-9169-z.

Allen, G.H., Pavelsky, T.M., 2018. Global extent of rivers and streams. Science 361 (6402), 585–588. https://www.science.org/doi/10.1126/science.aat0636.

Amani, M., Brisco, B., Afshar, M., Mirmazloumi, S.M., Mahdavi, S., Mirzadeh, S.M.J., Huang, W.M., Granger, J., 2019. A generalized supervised classification scheme to produce provincial wetland inventory maps: an application of Google Earth Engine for big geo data processing. Big Earth Data 3 (4), 378–394. https://doi.org/10.1080/20964471.2019.1690404.

Asselen, S.V., Verburg, P.H., Vermaat, J.E., Janse, J.H., 2013. Drivers of wetland conversion: a global meta-analysis. PLoS ONE 8, 81292. https://doi.org/10.1371/journal.pone.0081292.

Brown, C.F., Brumby, S.P., Guzder-Williams, B., Birch, T., Hyde, S.B., Mazzariello, J., Czerwinski, W., Pasquarella, V.J., Haertel, R., Ilyushchenko, S., Schwehr, K., Weisse, M., Stolle, F., Hanson, C., Guinan, O., Moore, R., Tait, A.M., 2022. Dynamic world, near real-time global 10 m land use land cover mapping. Sci. Data 9, 251. https://doi.org/10.1038/s41597-022-01307-4.

Cai, B.W., Shao, Z.F., Fang, S.H., Huang, X., Tang, Y., Zheng, M.C., Zhang, H., 2022. The Evolution of urban agglomerations in China and how it deviates from Zipf's law. Geo-Spat Inf. Sci. 1–11. https://doi.org/10.1080/10095020.2022.2083527.

Chen, J., Chen, J., Liao, A.P., Cao, X., Chen, L.J., Chen, X.H., He, C.Y., Han, G., Peng, S., Lu, M., Zhang, W.W., Tong, X.H., Mills, J., 2015. Global land cover mapping at 30 m resolution: a POK-based operational approach. ISPRS J. Photogramm. Remote Sens. 103, 7–27. https://doi.org/10.1016/j.isprsjprs.2014.09.002.

Conners, R.W., Trivedi, M.M., Harlow, C.A., 1984. Segmentation of a high-resolution urban scene using texture operators. Comput. Vis. Graphics Image Process. 25 (3), 273–310. https://doi.org/10.1016/0734-189X(84)90197-X.

Coumou, D., Rahmstorf, S., 2012. A decade of weather extremes. Nat. Clim. Chang. 2, 491–496. https://doi.org/10.1038/nclimate1452.

Dang, C.Y., Shao, Z.F., Huang, X., Qian, J.X., Cheng, G., Ding, Q., Fan, Y.W., 2022. Assessment of the importance of increasing temperature and decreasing soil moisture on global ecosystem productivity using solar-induced chlorophyll fluorescence. Glob. Chang. Biol. 28 (6), 2066–2080. https://doi.org/10.1111/gcb.16043.

Daniele, Z., Ruben, V.D.K., Wanda, D.K., Niels, S., Carsten, B., Ralf, Q., Jan, W., Alex, G., Audrey, P., Sylvain, V., Oliver, C., Maurizio, S., Steffen, F., Ivelina, G., Myroslava, L., Sarah, C., Martin, H., Linlin, L., Nandin-Erdene, T., Fabrizio, R., Olivier, A., 2021. ESA WorldCover 10 m 2020 v100. https://doi.org/10.5281/zenodo.5571936.

Das, A., Basu, T., 2020. Assessment of peri-urban wetland ecological degradation through importance-performance analysis (IPA): a study on Chatra Wetland, India. Ecol. Indic. 114, 106274 https://doi.org/10.1016/j.ecolind.2020.106274.

Feng, L., Hu, C.M., Chen, X.L., Cai, X.B., Tian, L.Q., Gan, W.X., 2012. Assessment of inundation changes of Poyang Lake using MODIS observations between 2000 and 2010. Remote Sens. Environ. 121, 80–92. https://doi.org/10.1016/j.rse.2012.01.014.

Feng, K.D., Mao, D.H., Qiu, Z.Q., Zhao, Y.X., Wang, Z.M., 2022. Can time-series Sentinel images be used to properly identify wetland plant communities? GISci. Remote Sens. 59 (1), 2202–2216. https://doi.org/10.1080/15481603.2022.2156064.

Gong, P., Niu, Z.G., Cheng, X., Zhao, K.Y., Zhou, D.M., Guo, J.H., Liang, L., Wang, X.F., Li, D.D., Huang, H.B., Wang, Y., Wang, K., Li, W.N., Wang, X.W., Ying, Q., Yang, Z.Z., Ye, Y.F., Li, Z., Zhuang, D.F., Chi, Y.B., Zhou, H.Z., Yan, J., 2010. China's wetland change (1990–2000) determined by remote sensing. Sci. China Earth Sci. 53, 1036–1042. https://doi.org/10.1007/s11430-010-4002-3.

Gong, P., Li, X.C., Wang, J., Bai, Y.Q., Chen, B., Hu, T.Y., Liu, X.P., Xu, B., Yang, J., Zhang, W., Zhou, Y.Y., 2020. Annual maps of global artificial impervious area (GAIA) between 1985 and 2018. Remote Sens. Environ. 236, 111510 https://doi.org/10.1016/j.rse.2019.111510.

Guan, X.W., Zeng, M., 2022. Analysis and insights on the characteristics of dry water in Yangtze River Basin in 2022. Yangtze River 53 (12), 1–5+36 (in Chinese). https://link.cnki.net/doi/10.16232/j.cnki.1001-4179.2022.12.001.

Hadeel, A., Jabbar, M., Chen, X.L., 2009. Application of remote sensing and GIS to the study of land use/cover change and urbanization expansion in Basrah province, southern Iraq. Geo-Spat. Inf. Sci. 12 (2), 135–141. https://doi.org/10.1007/s11806-009-0244-7.

Haralick, R.M., Shanmugam, K., Dinstein, I.H., 1973. Textural features for image classification. IEEE Trans. Syst. Man Cybern. SMC-3 (6), 610–621. https://doi.org/10.1109/TSMC.1973.4309314.

Harrison, M.D., Groffman, P.M., Mayer, P.M., Kaushal, S.S., Newcomer, T.A., 2011. Denitrification in alluvial wetlands in an urban landscape. J. Environ. Qual. 40 (2), 634–646. https://doi.org/10.2134/jeq2010.0335.

He, C.Y., Liu, Z.F., Tian, J., Ma, Q., 2014. Urban expansion dynamics and natural habitat loss in China: a multiscale landscape perspective. Glob. Chang. Biol. 20, 2886–2902. https://doi.org/10.1111/gcb.12553.

Huang, C.B., Teng, M.J., Zeng, L.X., Zhou, Z.X., Xiao, W.F., Zhu, J.H., Wang, P.C., 2018. Long term changes of land use/cover in the Three Gorges Reservoir Area of the Yangtze River, China. J. Appl. Ecol. 29, 1585–1596 (in Chinese). 10.13287/j.1001-9332.201805.012.

Huete, A.R., Liu, H.Q., Batchily, K., Leeuwen, W.V., 1997. A comparison of vegetation indices over a global set of TM images for EOS-MODIS. Remote Sens. Environ. 59 (3), 440–451. https://doi.org/10.1016/S0034-4257(96)00112-5.

Jantz, P., Goetz, S., Jantz, C., 2005. Urbanization and the loss of resource lands in the Chesapeake Bay Watershed. Environ. Manag. 36, 808–825. https://doi.org/10.1007/s00267-004-0315-3.

Jia, M.M., Wang, Z.M., Mao, D.H., Ren, C.Y., Wang, C., Wang, Y.Q., 2021. Rapid, robust, and automated mapping of tidal flats in China using time series Sentinel-2 images and Google Earth Engine. Remote Sens. Environ. 255, 112285 https://doi.org/10.1016/j.rse.2021.112285.

Jia, J.W., Wang, D., Xu, W.F., Liu, X., 2023. Comprehensive assessment and causal analysis of drought in Poyang Lake Basin in 2022. Yangtze River 54 (02), 36–42 (in Chinese). https://link.cnki.net/doi/10.16232/j.cnki.1001-4179.2023.02.006.

Karra, K., Kontgis, C., Statman-Weil, Z., Mazzariello, J.C., Mathis, M., Brumby, S.P., 2021. Global land use/land cover with Sentinel 2 and deep learning. In: 2021 IEEE International Geoscience and Remote Sensing Symposium IGARSS, Brussels, Belgium, pp. 4704–4707. https://doi.org/10.1109/IGARSS47720.2021.9553499.

Keddy, P.A., Fraser, L.H., Solomeshch, A.I., Junk, W.J., Campbell, D.R., Arroyo, M.T.K., Alho, C.J.R., 2009. Wet and wonderful: the world's largest wetlands are conservation priorities. BioScience 59 (1), 39–51. https://doi.org/10.1525/bio.2009.59.1.8.

Khandelwal, A., Karpatne, A., Ravirathinam, P., Ghosh, R., Wei, Z.H., Dugan, H.A., Hanson, P.C., Kumar, V., 2022. ReaLSAT, a global dataset of reservoir and lake surface area variations. Sci. Data 9, 356. https://doi.org/10.1038/s41597-022-01449-5.

Li, B., Wan, R.R., Yang, G.S., Tan, Z.Q., Wang, D.C., Wu, X.H., 2022. Investigating spatiotemporal dynamics of Lake Poyang wetland for the recent century. J. Lake Sci. 34 (3), 1018–1029. https://doi.org/10.18307/2022.0325.

Liu, X.H., Dong, G.H., Wang, X.G., Xue, Z.S., Jiang, M., Lu, X.G., Zhang, Y., 2013. Characterizing the spatial pattern of marshlands in the Sanjiang Plain, Northeast China. Ecol. Eng. 53, 335–342. https://doi.org/10.1016/j.e coleng.2012.12.071.

Luo, Y., Lu, Y.H., Fu, B.J., Zhang, Q.J., Li, T., Hu, W.Y., Comber, A., 2019. Half century change of interactions among ecosystem services driven by ecological restoration: quantification and policy implications at a watershed scale in the Chinese Loess Plateau. Sci. Total Environ. 651, 2546–2557. https://doi.org/10.1016/j.scit otenv.2018.10.116.

Mahdavi, S., Salehi, B., Granger, J., Amani, M., Brisco, B., Huang, W., 2017. Remote sensing for wetland classification: a comprehensive review. GISci. Remote Sens. 55 (5), 623–658.

Mao, D.H., Wang, Z.M., Du, B.J., Li, L., Tian, Y.L., Jia, M.M., Zeng, Y., Song, K.S., Jiang, M., Wang, Y.Q., 2020. National wetland mapping in China: a new product resulting from objectbased and hierarchical classification of landsat 8 OLI images. ISPRS J. Photogramm. Remote Sens. 164, 11–25. https://doi.org/10.1016/j.isprsjprs.2020.03.020.

Mcfeeters, S.K., 1996. The use of the Normalized Difference Water Index (NDWI) in the delineation of open water features. Int. J. Remote Sens. 17, 1425–1432. https://doi.org/10.1080/01431169608948714.

Messager, M.L., Lehner, B., Grill, G., Nedeva, I., Schmitt, O., 2016. Estimating the volume and age of water stored in global lakes using a geo-statistical approach. Nat. Commun. 7, 13603. https://doi.org/10.1038/ncomms13603.

Mitsch, W.J., Bernal, B., Hernandez, M.E., 2015. Ecosystem services of wetlands. Int. J. Biodivers. Sci. Ecosyst. Serv. Manag. 11, 1–4. https://doi.org/10.1080/21513732.2015.1006250.

Murray, N.J., Phinn, S.R., DeWitt, M., Ferrari, R., Johnston, R., Lyons, M.B., Clinton, N., Thau, D., Fuller, R.A., 2019. The global distribution and trajectory of tidal flats. Nature 565, 222–225. https://doi.org/10.1038/s41586-018-0805-8.

Mutanga, O., Adam, E., Cho, M.A., 2012. High density biomass estimation for wetland vegetation using WorldView-2 imagery and random forest regression algorithm. Int. J. Appl. Earth Obs. Geoinf. 18, 399–406. https://doi.org/10.1016/j.jag.2012.03.012.

Niu, Z.G., Gong, P., Cheng, X., Guo, J.H., Wang, L., Huang, H.B., Shen, S.Q., Wu, Y.Z., Wang, X.F., Wang, X.W., Ying, Q., Liang, L., Zhang, L.N., Wang, L., Yao, Q., Yang, Z. Z., Guo, Z.Q., Dai, Y.J., 2009. Geographical characteristics of China's wetlands derived from remotely sensed data. Sci. China Ser. D-Earth Sci. 52, 723–738. https://doi.org/10.1007/s11430-009-0075-2.

Pan, Y.L., Xu, X.D., Long, J.P., Lin, H., 2022. Change detection of wetland restoration in China's Sanjiang National Nature Reserve using STANet method based on GF-1 and GF-6 images. Ecol. Indic. 145, 109612. https://doi.org/10.1016/j.ecolind.2022.109612.

Pekel, J.F., Cottam, A., Gorelick, N., Belward, A.S., 2016. High mapping of global surface water and its long-term changes. Nature 540, 418–422. https://doi.org/10.1038/nature20584.

Rapinel, S., Fabre, E., Dufour, S., Arvor, D., Mony, C., Hubert-Moy, L., 2019. Mapping potential, existing and efficient wetlands using free remote sensing data. J. Environ. Manag. 247, 829–839. https://doi.org/10.1016/j.jenvman.2019.06.098.

Rikimaru, A., 1996. Landsat TM data processing guide for forest canopy density mapping and monitoring model. In: ITTO Workshop on Utilization of Remote Sensing in Site Assessment and Planning for Rehabilitation of Logged-over Forest. July 30–August 1, Bangkok, Thailand, 1996.

Rouse, J.W., Haas, R.H., Schell, J.A., Deering, D.W., 1973. Monitoring vegetation systems in the great plains with ERTS. In: Third ERTS Symposium, NASA SP-351, NASA Washington, DC, vol. 1, pp. 309–317.

Sahraei, R., Ghorbanian, A., Kanani-Sadat, Y., Jamali, S., Homayouni, S., 2023. Mangrove plantation suitability mapping by integrating multi criteria decision making geospatial approach and remote sensing data. Geo-Spat Inf Sci. 1–19. https://doi.org/10.1080/10095020.2023.2167615.

Savard, J.P.L., Clergeau, P., Mennechez, G., 2000. Biodiversity concepts and urban ecosystems. Landsc. Urban Plan. 48, 131–142. https://doi.org/10.1016/S0169-2046(00)00037-2.

Shao, Z.F., Li, C.M., Li, D.R., Altan, O., Zhang, L., Ding, L., 2020. An accurate matching method for projecting vector data into surveillance video to monitor and protect cultivated land. ISPRS Int. J. Geo-Inf. 9 (7), 448. https://doi.org/10.3390/ijgi9070448.

Sheng, Y.W., Song, C.Q., Wang, J.D., Lyons, E.A., Knox, B.R., Cox, J.S., Gao, F., 2016. Representative lake water extent mapping at continental scales using multi-temporal Landsat-8 imagery. Remote Sens. Environ. 185, 129–141. https://doi.org/10.1016/j.rse.2015.12.041.

Sun, R., Chen, A., Chen, L., Lü, Y., 2012. Cooling effects of wetlands in an urban region: the case of Beijing. Ecol. Indic. 20 (9), 57–64. https://doi.org/10.1016/j.ecolind.2012.02.006.

Wang, X.L., Ning, L.M., Yu, J., Xiao, R., Li, T., 2008. Changes of urban wetland landscape pattern and impacts of urbanization on wetland in Wuhan City. Chin. Geogr. Sci. 18, 47–53. https://doi.org/10.1007/s11769-008-0047-z.

Wang, Z.M., Wu, J.G., Madden, M., Mao, D.H., 2012. China's wetlands: conservation plans and policy impacts. AMBIO 41, 782–786. https://doi.org/10.1007/s13280-012-0280-7.

Wang, X.X., Xiao, X.M., Zou, Z.H., Chen, B.Q., Ma, J., Dong, J.W., Doughty, R.B., Zhong, Q.Y., Qin, Y.W., Dai, S.Q., Li, X.P., Zhao, B., Li, B., 2020a. Tracking annual changes of coastal tidal flats in China during 1986–2016 through analyses of Landsat images with Google Earth Engine. Remote Sens. Environ. 238, 110987 https://doi.org/10.1016/j.rse.2018.11.030.

Wang, X.X., Xiao, X.M., Zou, Z.H., Hou, L.Y., Qin, Y.W., Dong, J.W., Doughty, R.B., Chen, B.Q., Zhang, X., Chen, Y., Ma, J., Zhao, B., Li, B., 2020b. Mapping coastal wetlands of China using time series Landsat images in 2018 and Google Earth Engine. ISPRS J. Photogramm. Remote Sens. 163, 312–326. https://doi.org/10.1016/j.isprsjp rs.2020.03.014.

Wang, X.X., Xiao, X.M., Qin, Y.W., Dong, J.W., Wu, J.H., Li, B., 2022a. Improved maps of surface water bodies, large dams, reservoirs, and lakes in China. Earth Syst. Sci. Data 14, 3757–3771. https://doi.org/10.5194/essd-14-3757-2022.

Wang, X.Y., Jiang, W.G., Peng, K.F., Li, Z., Rao, P.A., 2022b. A framework for fine classification of urban wetlands based on random forest and knowledge rules: taking the wetland cities of Haikou and Yinchuan as examples. GISci. Remote Sens. 59 (1), 2144–2163. https://doi.org/10.1080/15481603.2022.2152926.

Wang, M., Mao, D.H., Xiao, X.M., Song, K.S., Jia, M.M., Ren, C.Y., Wang, Z.M., 2023. Interannual changes of coastal aquaculture ponds in China at 10-m spatial resolution during 2016–2021. Remote Sens. Environ. 284, 113347 https://doi.org/10.1016/j.rse.2022.113347.

Wu, F.L., Zhou, D.M., Hu, J.M., 2007. Approach on ecological planning of urban wetland on changes of landscape patterns. Resour. Environ. Yangtze Basin, 16(3), 368–372 (in Chinese). https://link.cnki.ne t/doi/https://doi.org/10.3969/j.issn.1004-8227.2007.03.020.

Xing, H.Q., Niu, J.G., Feng, Y.Y., Hou, D.Y., Wang, Y., Wang, Z.Q., 2023. A coastal wetlands mapping approach of Yellow River Delta with a hierarchical classification and optimal feature selection framework. Catena 223, 106897. https://doi.org/10.1016/j.catena.2022.106897.

Xu, H.Q., 2006. Modification of normalised difference water index (NDWI) to enhance open water features in remotely sensed imagery. Int. J. Remote Sens. 27, 3025–3033. https://doi.org/10.1080/01431160600589179.

Xu, H.Q., 2008. A new index for delineating built-up land features in satellite imagery. Int. J. Remote Sens. 29 (14), 4269–4276. https://doi.org/10.1080/01431160802039957.

Xu, K., Kong, C.F., Liu, G., Wu, C.L., Deng, H.B., Zhang, Y., Zhuang, Q.L., 2010. Changes of urban wetlands in Wuhan, China, from 1987 to 2005. Prog. Phys. Geogr. 34 (2), 207–220. https://doi.org/10.1177/0309133309360626.

Xu, C., Zhang, S.S., Zhao, B.F., Liu, C., Sui, H.G., Yang, W., Mei, L.Y., 2022. SAR image water extraction using the attention U-net and multi-scale level set method: flood monitoring in South China in 2020 as a test case. Geo-Spat Inf. Sci. 25 (2), 155–168. https://doi.org/10.1080/10095020.2021.1978275.

Xue, Z.S., Hou, G.L., Zhang, Z.S., Lyu, X.G., Jiang, M., Zou, Y.C., Shen, X.J., Wang, J., Liu, X.H., 2019. Quantifying the cooling-effects of urban and peri-urban wetlands using remote sensing data: case study of cities of Northeast China. Landsc. Urban Plan. 182, 92–100. https://doi.org/10.1016/j.landurbplan.2018.10.015.

Yang, J., Huang, X., 2021. The 30 m annual land cover dataset and its dynamics in China from 1990 to 2019. Earth Syst. Sci. Data 13, 3907–3925. https://doi.org/10.5194/essd-13-3907-2021.

Yue, L.W., Li, B.G., Zhu, S., Yuan, Q.Q., Shen, H.F., 2023. A fully automatic and high-accuracy surface water mapping framework on Google Earth Engine using Landsat time-series. Int. J. Digit. Earth 16 (1), 210–233. https://doi.org/10.1080/17538947.2023.2166606.

Zeng, L., Chen, G.Q., Tang, H.S., Wu, Z., 2011. Environmental dispersion in wetland flow. Commun. Nonlinear Sci. Numer. Simul. 16, 206–215. https://doi.org/10.1016/j.cnsns.2010.02.019.

Zhang, K., Yu, Z., Li, X., Zhou, W., Zhang, D., 2007. Land use change and land degradation in China from 1991 to 2001. Land Degrad. Dev. 18, 209–219. https://doi.org/10.1002/ldr.757.

Zhang, J., Hu, Q.W., Li, Y.K., Li, H.D., Li, J.Y., 2021a. Area, lake-level and volume variations of typical lakes on the Tibetan Plateau and their response to climate change, 1972–2019. Geo-Spat Inf. Sci. 24 (3), 458–473. https://doi.org/10.1080/10095020.2021.1940318.

Zhang, X., Liu, L.Y., Chen, X.D., Gao, Y., Xie, S., Mi, J., 2021b. GLC_FCS30: global land-cover product with fine classification system at 30 m using time-series landsat imagery. Earth Syst. Sci. Data 13, 2753–2776. https://doi.org/10.5194/essd-13-2753-2021.

Zhang, Z., Xu, N., Li, Y.F., Li, Y., 2022. Sub-continental-scale mapping of tidal wetland composition for East Asia: a novel algorithm integrating satellite tide-level and phenological features. Remote Sens. Environ. 269, 112799 https://doi.org/10.1016/j.rse.2021.112799.

Zhang, W., Hu, B.X, Brown, G., Meyer, S., 2023a. Beaver pond identification from multi-temporal and multi- sourced remote sensing data. Geo-Spat Inf Sci. 1–15. https://doi.org/10.1080/10095020.2023.2183144.

Zhang, X., Liu, L.Y., Zhao, T.T., Chen, X.D., Lin, S.R., Wang, J.Q., Mi, J., Liu, W.D., 2023b. GWL_FCS30: global 30 m wetland map with fine classification system using multi-sourced and time-series remote sensing imagery in 2020. Earth Syst. Sci. Data 15, 265–293. https://doi.org/10.5194/essd-2022-180.

Zhao, C.P., Qin, C.Z., 2020. 10-m-resolution mangrove maps of China derived from multi-source and multi-temporal satellite observations. ISPRS J. Photogramm. Remote Sens. 169, 389–405. https://doi.org/10.1016/j.isprsjprs.2020.10.001.

Zhao, C.P., Jia, M.M., Wang, Z.M., Mao, D.H., Wang, Y.Q., 2023. Toward a better understanding of coastal salt marsh mapping: a case from China using dual-temporal images. Remote Sens. Environ. 295, 113664 https://doi.org/10.1016/j.rse.2023.113664.